ChemElectroChem

Research Article
doi.org/10.1002/celc.202201164

Chemistry Europe
European Chemical Societies Publishing

www.chemelectrochem.org

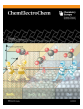

Redox-Stabilized Sn/SnO_2 Nanostructures for Efficient and Stable CO_2 Electroreduction to Formate

Haoyang Jiang[+],[a] Ziqi Fan[+],[a] Mingzhe Zhang[+],[a] Shuyi Guo[+],[b] Le Li,[a] Xiaohan Yu,[a] Zhaoyang Liu,[a] Wei Wang,[b] Hao Dong,*[b] and Miao Zhong*[a]

Electroreduction of CO_2 (CO_2R) to formate enables the storage of renewable electricity in liquid chemical bonds in an efficient manner. However, hydrogen evolution competes with CO_2R, decreasing Faradaic efficiency (FE) and energy efficiency (EE) for formate production, particularly under acidic and neutral conditions. The deterioration of the catalysts during CO_2R further hinders long-term and effective operation. To overcome these challenges, we fabricate nanostructured Sn/SnO_2 through physical evaporation and wet-chemical etching, improving the CO_2-to-formate conversion with finely tuned *OCHO adsorption. The in-situ formation of Sn/SnO_2 surfaces during CO_2R stabilizes the active sites for reliable formate production across a broad range of electrolyte pH from base to neutral. Our results show a 94% CO_2R-to-formate FE and a 58% formate cathodic EE at 100 mA cm^{-2} in 1 M KOH over 70 hours of continuous operation. Under neutral conditions (pH = 7), the CO_2-to-formate conversion remains stable for 100 h with a selectivity of > 90%.

Introduction

The extensive use of fossil fuels has led to increased carbon dioxide (CO_2) emissions and environmental pollution, urging the development of efficient carbon capture, utilization, and storage technologies.[1] Electrochemical CO_2 reduction (CO_2R) using renewable electricity is a promising approach to producing chemical raw materials.[2] As a liquid product, formate ($HCOO^-$) is desirable because the electrochemical production of $HCOO^-$ only involves two-electron transfers, enabling the high energy value of the process.[3]

Currently, p-block metals, including Sn, Bi, and Pb, have been studied for CO_2-to-formate conversion due to their appropriate O binding affinity to the key *OCHO intermediate.[4] Simultaneously, the weak adsorption of *COOH intermediate on p-block metals hinders the CO_2R to CO, CH_4, and C_{2+} conversion.[5] Among the p-block metals, Sn has a relatively strong binding to *OCHO, favoring the first-step proton-coupled electron transfer in the CO_2R-to-formate conversion.[4c] However, the modest H^+ binding on the Sn and Sn-based catalysts makes it challenging to suppress hydrogen evolution reaction (HER) and optimize formate production.[5d] At a high current density of over 100 mA cm^{-2}, most reported formate Faradaic efficiencies (FEs) using metallic Sn and Sn-based electrodes are lower than 80%.[6,7]

Recent studies have focused on improving the CO_2R-to-formate selectivity and energy efficiency by using phase-segregated catalysts and core-shell nanostructured catalysts. Chen et al. reported that Bi nanoparticles on Sn nanosheets increase the electrochemical CO_2 reduction to formate with Faradaic efficiency (FE) of 96% at a current density of about 55 mA cm^{-2} at −1.1 V vs. reversible hydrogen electrode (V_{RHE}).[8] Wang et al. reported that a $Sn_{2.7}Cu$ catalyst achieves a high current density of 406.7 ± 14.4 mA cm^{-2} with a formate FE of 80% at −0.70 V_{RHE}.[9] Jiao et al. synthesized Ag–Sn core-shell electrocatalysts, exhibiting a formate FE of ~80% at a formate partial current density of ~16 mA cm^{-2} at −0.8 V_{RHE}.[10] Although much progress has been made in alkaline electrolytes, the CO_2 utilization efficiency remains low due to carbonate formation at high pHs. Therefore, to improve CO_2 utilization, CO_2R should be operated under neutral or acidic conditions. Additionally, the catalysts need to be long-term stable during CO_2-to-formate production for practical application.

In this study, large-scale nanostructured Sn/SnO_2 catalysts were fabricated on polytetrafluoroethylene (PTFE) gas diffusion electrodes using physical evaporation and wet chemical etching. Computational studies showed that Sn/SnO_2 surfaces fine-tune the binding energy of *OCHO to enhance the CO_2-to-formate conversion over HER. Scanning electron microscopy (SEM), X-ray powder diffraction (XRD), and X-ray photoelectron spectroscopy (XPS) depth profile analyses revealed the stable, active Sn/SnO_2 sites throughout the electrochemical formate production across a broad range of electrolyte pH, from base to neutral. The formate FE was > 94% at a current density of 100 mA cm^{-2} over 70 hours in 1 M KOH. Under neutral con-

[a] H. Jiang,[+] Z. Fan,[+] M. Zhang,[+] L. Li, X. Yu, Z. Liu, Prof. M. Zhong
College of Engineering and Applied Sciences
National Laboratory of Solid State Microstructures
Jiangsu Key Laboratory of Artificial Functional Materials
Nanjing University
Nanjing 210023 (P. R. China)
E-mail: miaozhong@nju.edu.cn
[b] S. Guo,[+] Prof. W. Wang, Prof. H. Dong
Kuang Yaming Honors School and Institute for Brain Sciences
Nanjing University, Nanjing 210023 (P. R. China)
E-mail: donghao@nju.edu.cn

[+] These authors contributed equally to this work.

Supporting information for this article is available on the WWW under https://doi.org/10.1002/celc.202201164

ditions (pH = 7), the formate production was stable over 100 h, with selectivity exceeding 90%.

Results and Discussion

Material synthesis and characterization

The nanostructured Sn/SnO_2 catalysts were prepared through thermal evaporation and wet-chemical etching (Figure 1a).[4a,11] First, phase-segregated $Sn_{1-x}Zn_x$ ($x = 0.05$, 0.15, 0.5) catalysts with different Sn/Zn molar ratios were evaporated onto the PTFE substrates (Figure 1b and S1). The XRD patterns only showed metallic Sn and Zn phases in the as-evaporated samples (Figure S8). The XPS spectra in Figure 1c showed Sn^{4+} (494.3 eV, 485.5 eV), Sn^0 (491.8 eV, 483.5 eV), and Zn^0 (1044.5 eV, 1021.4 eV) with the as-evaporated catalysts. The peak at 498 eV represented the Zn Auger peak. The XPS result indicated the presence of SnO_2 on the surfaces. Compared to Sn, Zn was easily dissolved in strong acid and alkaline solutions; therefore, wet chemical etching was first carried out to remove Zn from $Sn_{1-x}Zn_x$ ($x = 0.05$, 0.15, 0.5) using 0.1 M HCl (details in Supporting Information). After wet etching, the $Sn_{1-x}Zn_x$ ($x = 0.05$, 0.15, 0.5) catalysts were utilized in CO_2R pre-electrolysis in 1 M KOH at 100 mA cm^{-2} for one hour. After pre-electrolysis, a series of Sn/SnO_2 nanostructured catalysts were obtained from $Sn_{1-x}Zn_x$ ($x = 0.05$, 0.15, 0.5) catalysts and denoted Sn/SnO_2 NS-1, Sn/SnO_2 NS-2, and Sn/SnO_2 NS-3, respectively. SEM images showed that the morphologies changed from a dense particle framework with as-evaporated $Sn_{0.95}Zn_{0.05}$ to a porous structure with Sn/SnO_2 NS-1 (Figure 1b, 1d). The particle size in Sn/SnO_2 NS-1 was ~50–100 nm, while Sn/SnO_2 NS-2 and Sn/SnO_2 NS-3 showed larger particle sizes of ~500–1000 nm (Figure S2). As shown in the XPS spectra of Sn/SnO_2 NS-1, Sn^{4+} 3d signals

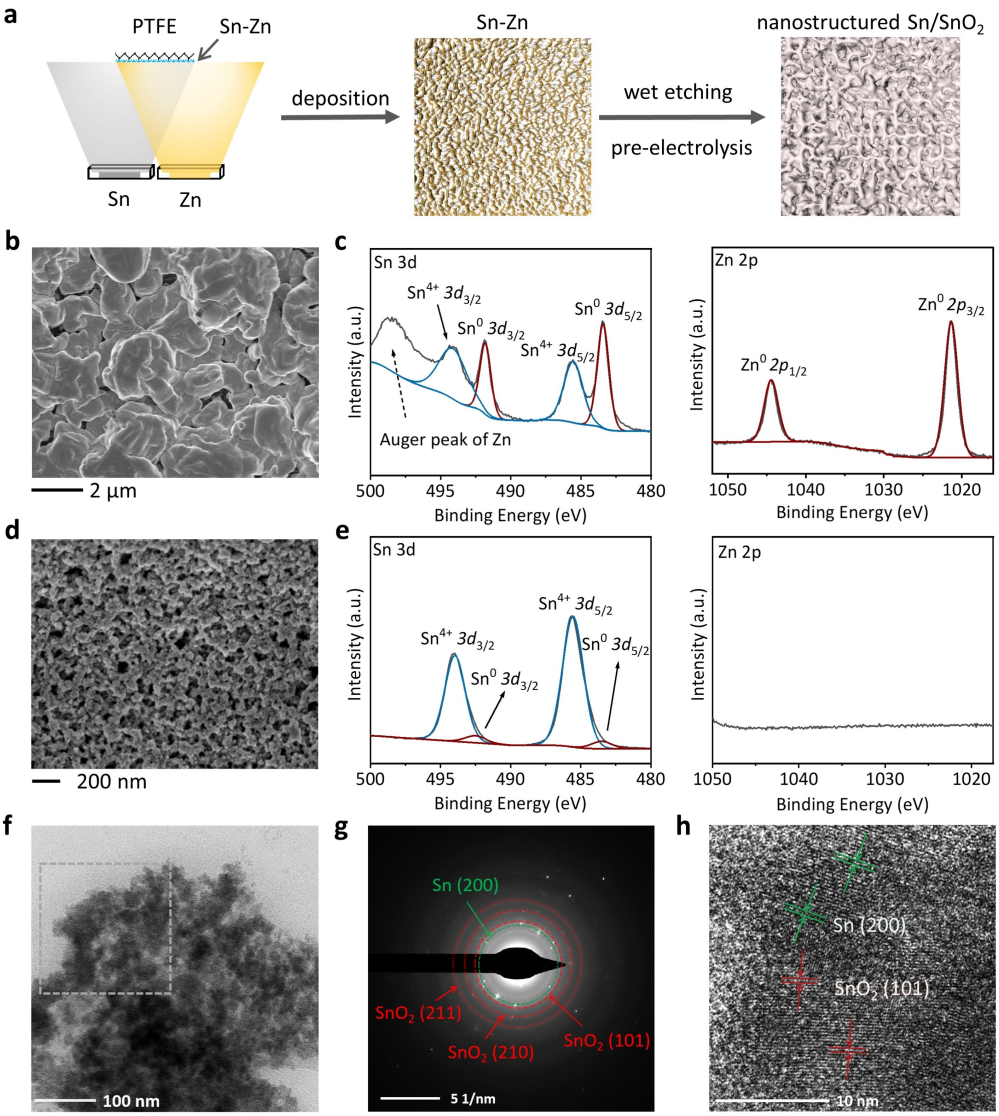

Figure 1. Structural and elemental analyses of $Sn_{0.95}Zn_{0.05}$ and Sn/SnO_2 NS-1 catalysts. (a) Schematic of thermal evaporation and wet chemical etching to prepare nanostructured Sn/SnO_2. (b) SEM image, and (c) XPS spectra of the as-evaporated $Sn_{0.95}Zn_{0.05}$. (d) SEM image, (e) XPS spectra, (f) TEM image, (g) SAED pattern, and (h) HRTEM image of the Sn/SnO_2 NS-1.

increased largely, and the Zn 2p signals disappeared (Figure 1e and S9). This suggested that the surface Zn was completely removed.

To examine the crystallography and element distribution in the nanostructured Sn/SnO_2 NS-1, transmission electron microscopy (TEM), transmission electron microscopy-energy dispersive X-ray spectroscopy (TEM-EDX), and high-resolution transmission electron microscopy (HRTEM) analyses were performed. As shown in Figure 1f, a collection of nanocrystals was observed for the Sn/SnO_2 NS-1 in the TEM analysis. The select area electron diffraction (SAED) pattern (Figure 1g) and HRTEM image (Figure 1h) visualized the formation of Sn and SnO_2 mixed catalyst layers in a polycrystalline nature, which agrees with the XRD results (Figure 3a).

Density functional theory (DFT) calculation

The reduction of CO_2 to $HCOO^-$ involves two proton-coupled electron transfer steps and a key intermediate *OCHO. The adsorption energy of *OCHO on catalysts determines the overall energy required for the reaction (Figure 2c). We then used DFT to calculate the adsorption energy of *OCHO on different surfaces of Sn (100), Sn (100)/SnO_2, SnO_2 (101)/Sn, and SnO_2 (101) surfaces (Figures 2c, S3, and S4). It is 0.35 eV, 0.42 eV, 0.51 eV, and 0.80 eV on Sn (100)/SnO_2, SnO_2 (101)/Sn, Sn (100), and SnO_2 (101) surfaces, respectively. This result suggests that the Sn/SnO_2 surfaces are more active for the CO_2 to $HCOO^-$ reduction than the pure Sn and SnO_2 surfaces.

CO_2R performance evaluation

To evaluate the CO_2R performance of the Sn/SnO_2 NS-1, Sn/SnO_2 NS-2, Sn/SnO_2 NS-3 and the control sample of pristine Sn, first, we carried out linear sweep voltammetry (LSV) measurements under the alkaline condition in 1 M KOH at pH = 14 in a flow cell from 0 to -2 V_{RHE} (Figure 2a). As shown in Figure 2b, the onset potential of Sn/SnO_2 NS-1 (-0.59 V_{RHE}) was more positive than that of Sn (-0.66 V_{RHE}). As shown in Figure 2b, electrochemical impedance spectroscopy (EIS) measurements confirmed that the interface resistance of Sn/SnO_2 NS-1 was lower than those of the Sn, Sn/SnO_2 NS-2, and Sn/SnO_2 NS-3 catalysts. The CO_2R product selectivity was analyzed by gas chromatography (GC) and ion chromatography (IC). The Sn/SnO_2 NS-1 showed $HCOO^-$ FEs over 90% at 100, 200, and

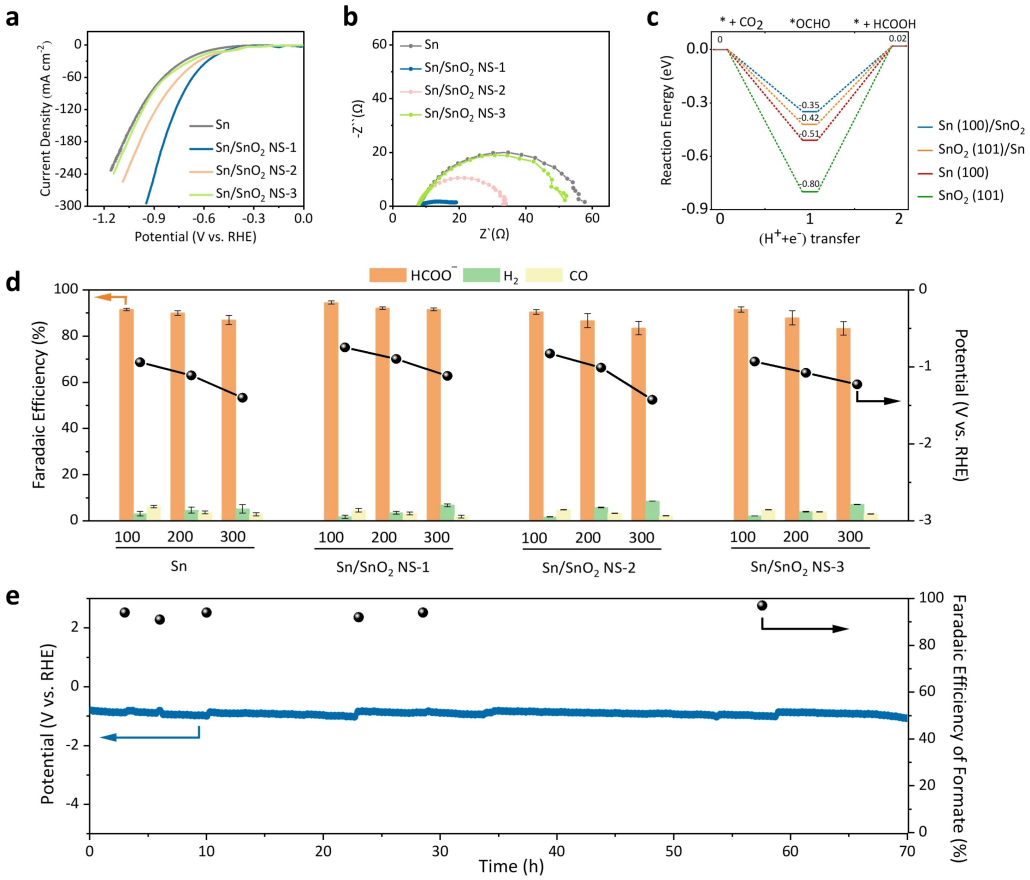

Figure 2. CO_2 electroreduction performance of the Sn/SnO_2 NS-1, Sn/SnO_2 NS-2, Sn/SnO_2 NS-3, and Sn catalysts in 1 M KOH. (a) LSV curves. (b) Electrochemical impedance spectroscopy results. (c) *OCHO adsorption energy on Sn (100)/SnO_2, SnO_2 (101)/Sn, Sn (100), SnO_2 (101) surfaces in the absence of the electrode potential (U = 0 V). Sn (100)/SnO_2 stands for a less oxidized Sn (100) surface containing 1.04% (molar ratio) SnO_2, and SnO_2 (101)/Sn represents a higher oxidized SnO_2 (101) surface containing 97.9% SnO_2. (d) Faradaic efficiency of $HCOO^-$, H_2, and CO at 100, 200, and 300 mA cm^{-2}. (e) Chronopotentiometry curve with formate FE in pH 14 at 100 mA cm^{-2}.

300 mA cm^{-2}, indicating that the Sn/SnO_2 NS-1 catalyst is selective for $HCOO^-$ production in a wide working potential window (Figure 2d). The $HCOO^-$ FE reached 94% at a current density of 100 mA cm^{-2} at a low applied potential of −0.75 V_{RHE}. As for the Sn/SnO_2 NS-2 and Sn/SnO_2 NS-3 catalysts, the $HCOO^-$ FEs are lower than 90%, while more than 10% of the products were H_2 and CO.

To assess the stability of the Sn/SnO_2 NS-1 catalyst during CO_2R, we conducted galvanostatic tests in 1 M KOH. As shown in Figure S5 and Figure 2e, Sn/SnO_2 NS-1 maintained the $HCOO^-$ FE exceeding 90% for more than 70 h at a current density of 100 mA cm^{-2}. The SEM images revealed that the porous structure of the Sn/SnO_2 NS-1 catalyst remained stable after 40-h and 70-h CO_2R tests (Figure 3a–c). Although the XPS spectra indicated the formation of SnO_2 layer on the catalyst surfaces after 1-h reaction (Figure 1e), the amount of SnO_2 is too small to be observed in the XRD pattern (Figure 3a). After 40-h and 70-h reactions, SnO_2 phases appeared in the XRD patterns (Figure 3b–c). This experimental result suggested that SnO_2 gradually grew with time, which allows a redox modulation between Sn and SnO_2. We suggest that this effectively contributes to long-term stability.

To further investigate the chemical compositions in the catalyst surface layers, we performed an XPS depth profile study toward the Sn/SnO_2 NS-1 catalyst after the 70-h reaction. As reported in previous studies,[11] the catalyst surfaces were easily oxidized when exposed to the air after being removed from the alkaline electrolyte. Therefore, we did a short pre-sputtering (120–240 s, ~5 nm) to clean up the top surface oxides formed in the air. As shown in Figure 3d, Sn^0 and Sn^{4+} were observed on the catalyst surface during three rounds of 240-s soft Ar etching (~5 nm etching thickness for each round) for Sn/SnO_2 NS-1 after the 70-h reaction. We estimated the Sn^{4+} and Sn^0 proportions (Figure S6 and Table S2). The result suggested that the ratio of Sn^{4+}/Sn^0 in the top surface layer was similar during the first three etchings, indicating the formation of a uniform Sn/SnO_2 layer on the catalyst surfaces. We further compared the potentiodynamic polarization curves of Sn/SnO_2 NS-1 after 1, 10, and 50-h reactions (Figure 3e). The corrosion potentials were similar, indicating that stable Sn/SnO_2 surfaces were formed.

Finally, we evaluated the CO_2R performance of Sn/SnO_2 NS-1, Sn/SnO_2 NS-2, Sn/SnO_2 NS-3, and pure Sn at pH 7. The 3 M KCl electrolyte was used to suppress HER and improve CO_2R. As shown in Figure 4c, the Sn/SnO_2 NS-1 catalyst exhibited the best electrocatalyst performance with the most positive onset potential compared to the control samples. We then evaluated the FEs of the gaseous and liquid products using Sn/SnO_2 NS-1 at 100–300 mA cm^{-2}, under which conditions the $HCOO^-$ FEs were above 90% (Figure 4d). At 100 mA cm^{-2}, the Sn/SnO_2 NS-1

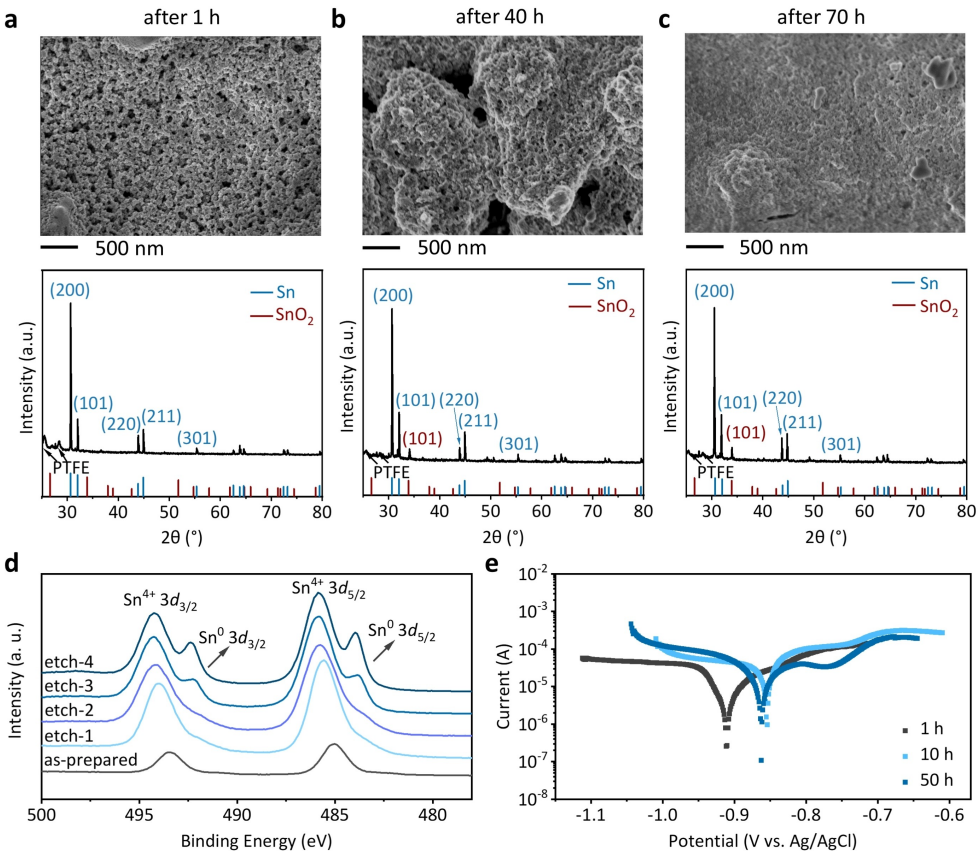

Figure 3. SEM, XRD, XPS depth profile, and potentiodynamic polarization studies of the Sn/SnO_2 NS-1 catalysts after 70-h of the stability test. (a–c) SEM and XRD results of the Sn/SnO_2 NS-1 catalysts after 1-h (a), 40-h (b), and 70-h (c) CO_2R stability test. (d) XPS depth profiles for the Sn/SnO_2 NS-1 after 70-h CO_2R reaction at 100 mA cm^{-2} in 1 M KOH. (e) The polarization curves of the Sn/SnO_2 NS-1 catalysts after 1-h, 10-h, and 50-h CO_2R reaction.

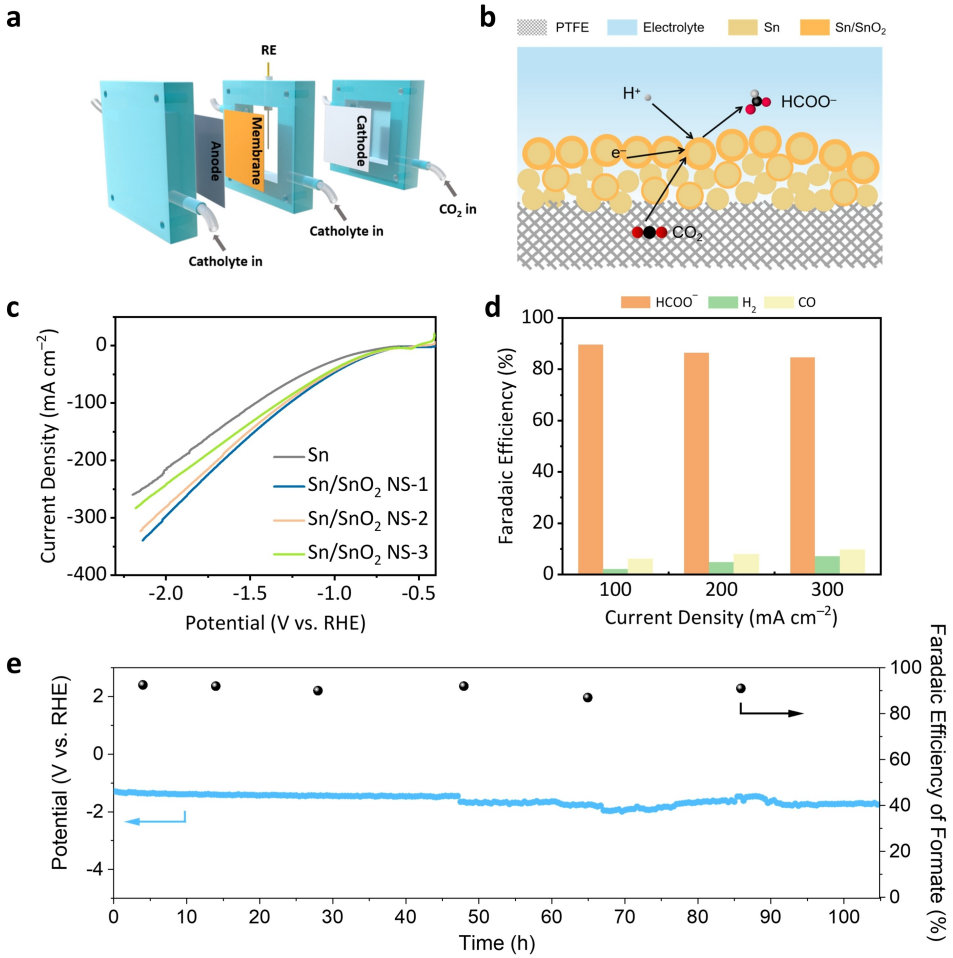

Figure 4. Electrochemical CO_2R stability of the Sn/SnO_2 NS-1 catalyst. (a) A flow-cell configuration. (b) Schematic of the reaction interfaces. (c) LSV curves of Sn/SnO_2 NS-1, Sn/SnO_2 NS-2, Sn/SnO_2 NS-3, and pure Sn at pH 7. (d) Faradaic efficiency of $HCOO^-$, H_2, and CO at 100, 200, and 300 mA cm^{-2} of Sn/SnO_2 NS-1 at pH 7. (e) CO_2R chronopotentiometry curve with formate FE at pH 7 at 100 mA cm^{-2}. The catholyte is 3 M KCl and the anolyte is 0.5 M $KHCO_3$.

catalyst was stable for over 100 hours with a $HCOO^-$ FE of >90% in a neutral electrolyte (Figure 4e). Compared to the reported Sn-based catalysts, the nanostructured Sn/SnO_2 improved the CO_2R performance in all the aspects of selectivity, current density, and stability under both neutral and alkaline conditions (Table S3).

Conclusion

In summary, we created active and selective Sn/SnO_2 nanocatalysts through evaporation and wet chemical etching. The CO_2-to-formate conversion was stable over 100 h with a selectivity of >90%, and H_2 and CO were suppressed to below 5–10% with 100-h stability under neutral conditions (pH 7). DFT calculation showed that Sn (100)/SnO_2 and SnO_2 (101)/Sn offered improved *OCHO binding to reduce the energy required for the CO_2-to-formate reaction. The Sn/SnO_2 interfaces were stable for extended CO_2R due to the self-redox modulation between Sn and SnO_2 in the electrolyte at cathodic potentials. Our findings show that surface redox modulation with optimized intermediate binding is an effective way to stabilize active sites and improve the activity for selective and stable CO_2 reduction.

Experimental Section

Synthesis

We fabricated $Sn_{1-x}Zn_x$ (x = 0.05, 0.15, 0.5) and Sn electrocatalysts using thermal evaporation (SKY-RH400). 3 g of Sn and 3 g of Zn metal particles were placed in two tungsten boats in the thermal evaporation chamber. Sn and Zn particles were evaporated at a pressure of 10^{-5} Pa. We controlled the evaporation rate by adjusting the current applied to the tungsten boat. A quartz crystal monitor was used to observe the thicknesses of the evaporated $Sn_{0.95}Zn_{0.05}$ films on PTFE substrates. After evaporation, we cut 2× 2 cm $Sn_{1-x}Zn_x$ (x = 0.05, 0.15, 0.5) samples, and carried out electrochemical etching using 0.1 M HCl electrolytes for 30 minutes with a stirring speed of 250 rpm for electrolytes, and then used flow cells for pre-electrolysis.

Characterization

Scanning electron microscope (SEM) images were taken using a HITACHI regulus 8100 at an accelerating voltage of 3 kV. XRD was carried out with a Bruker D8 Advance at a scanning rate of 9° min^{-1} in the 2θ range from 20° to 80°. Sn-PDF#04-0673 and SnO_2-PDF#41-1445 were used to contrast crystal planes. XPS studies were performed using PHI5000 VersaProbe. XPS depth profile studies were performed in the XPS chamber using Ar bombardment. Each etching time was 120–240 s which corresponds to ~5 nm per etching time. The binding energy data were calibrated relative to the C 1s signal at 284.6 eV.

Electrochemical experiments

All experiments were performed in flow cells using the three-electrode system. An Ag/AgCl (in saturated KCl) electrode was used as a reference electrode, a commercial nickel foam was used as a counter electrode, and the $Sn_{1-x}Zn_x$ (x = 0.05, 0.15, 0.5) and Sn catalysts were used as working electrodes. At pH 14, the anode and cathode electrolytes were 1 M KOH. At pH 7, the catholyte was 3 M KCl while the anolyte was 0.5 M $KHCO_3$. Metrohm Autolab potentiostat was used for the electrochemical measurements. The gas flow rate was controlled at 25 mL min^{-1} by a flow meter. The LSV studies were carried out in the potential range from 0 to $-2\ V_{RHE}$ with a scan rate of 50 mV s^{-1}. The electrochemical impedance spectroscopy was carried out to estimate the electrolyte resistance for IR compensation. The electrolyte resistance was measured at an open circuit potential in a frequency range from 10 MHz to 0.1 Hz with a voltage amplitude of 10 mV. All of the electrode potentials vs. the Ag/AgCl electrode were converted to the potentials vs. reversible hydrogen electrode (RHE) using Equation (1):

$$E_{RHE} = E_{Ag/AgCl} + 0.197 + 0.059 \times pH \quad (1)$$

Gas-phase products were measured using gas chromatography (GC2060, Shanghai Ruimin), According to the peak area, the FEs of the gas products were obtained using Equation (2):

$$FE = \frac{F \times z \times v \times n}{I \times t} \times 100\,\% \quad (2)$$

where F is the Faradaic efficiency constant, which is 96485 C mol^{-1}. z is the number of electrons required to reduce CO_2 to a CO or H_2 molecule. ν is the gas flow rate. n is the concentration of the gas products obtained by GC using 1 mL sample gas; the unit is mol mL^{-1}. I is the current applied to the sample; the unit is A.

Liquid product $HCOO^-$ was measured using ion chromatography (IC, SH-AC-11, Qingdao Shenghan). We first created a calibration curve using different concentrations of sodium formate (HCOONa). The $HCOO^-$ concentrations were set as 1, 2, 5, 10, 50, and 100 ppm (mg L^{-1}). Using the calibration curve, the $HCOO^-$ concentration in the electrolyte after the reaction was obtained. The $HCOO^-$ FE is calculated using Equation (3):

$$FE = \frac{F \times z \times V \times n}{45 \times I \times t} \times 100\,\% \quad (3)$$

where F is the Faradaic efficiency constant, which is 96485 C mol^{-1}. n is the concentration of $HCOO^-$ measured by the instrument based on the standard curve; the unit is mg L^{-1}. z is the number of electrons required for the reduction of CO_2 into $HCOO^-$. V is the volume of the catholyte.

The half-cell energy conversion efficiency (CEE) is calculated using Equation (4):

$$CEE_{formate} = \frac{(1.23 - E_{formate}) \times FE_{formate}}{1.23 - E_{cathode}} \quad (4)$$

where $E_{formate}$ is $-0.199\ V_{RHE}$ to form the formate in aqueous electrolytes. $FE_{formate}$ is the formate Faradaic efficiency. $E_{cathode}$ is the applied potential vs. RHE.

DFT calculation

Our experimental results show that the Sn (100) and SnO_2 (101) facets are the main crystallographic facets for the Sn and SnO_2 catalysts. Therefore, these facets were used to construct models for DFT calculations.

The cell parameters of Sn are a = b = 5.831 Å, c = 3.1821 Å. Starting from the unit cell, we constructed a 2×3×4 supercell and cut it into a (100) surface. The cell parameters of SnO_2 are a = b = 4.7456 Å, c = 3.1932 Å. We further built a 2×2×3 supercell and cut it into a (101) surface. We added a 20 Å vacuum layer in the c direction for both of the above systems. To construct the surfaces with different oxidation degrees, we added an oxygen atom to the Sn (100) surface and constructed a less oxidized Sn (100) surface containing 1.04% (molar ratio) SnO_2, denoted as Sn (100)/SnO_2; correspondingly, we removed an oxygen atom from the SnO_2 (101) surface to build a reduced SnO_2 (101) surface, denoted as SnO_2 (101)/Sn. Therefore, by comparing pure Sn (100), SnO_2 (101), and the two surfaces mentioned above, we can explore the effect of different oxidation states of the surface Sn on the catalytic performance.

All of the DFT calculations were performed using VASP.[12] The projector-augmented-wave (PAW) method was used for describing the electron-ion interactions.[13] The Perdew-Burke-Ernzerhof (PBE) functional was used;[14] The energy cutoff energy was set to 460 eV, and the k-points were set as 3×2×1. The width of the smearing, characterized by SIGMA, was set to 0.2 eV. The criterion of energy difference convergence was set to 10^{-4} eV, and no spin correction was applied. During the structure optimization, atoms from the top two layers were fully relaxed, while those from the bottom two layers were fixed. The open-source software vaspkit was used to calculate the thermodynamic and the density of states data.[15] The Gibbs free energy was obtained at 298 K and 1 atm, according to Equation (5):

$$G = H - TS = E_{DFT} + E_{ZPE} + \int_0^{298} C_v dT - TS \quad (5)$$

Where E_{DFT} is the electronic energy from DFT calculations, E_{ZPE} is the zero-point energy, the third term accounts for heat capacity, and the fourth term is the entropy correction obtained from frequency calculations. For gas molecules, the thermodynamic data, zero-point energy, specific heat capacity, and entropy were adopted from Klinkova, etc.[16] To correct the overestimation from DFT calculations, we followed the literature to apply corrections to the calculated energies of CO_2 (0.45 eV), HCOOH (0.20 eV), H_2 (−0.09 eV), and *OCHO (0.20 eV).[17] The solvent effect was calculated using vaspsol.[18]

Taking one elementary Reaction (6) as an example, the change of the Gibbs free energy of the reaction on the surface was calculated by Equation (7):

$$^{*}HCOO + H^{+} + e^{-} \rightleftharpoons HCOOH + ^{*} \quad (6)$$

$$\Delta G = G* + G_{HCOOH} - G*_{HCOO} - (G_{H^+} + G_{e^-}) = G* + G_{HCOOH} - G*_{HCOO} - \left(\frac{1}{2}G_{H_2} - eU\right) \quad (7)$$

Here, e and U represent the number of charges and the applied potential, respectively. In our calculations, we used a computational hydrogen electrode (CHE)[19] and set the applied potential to be zero, thus converting the free energy of a proton and an electron to half of the free energy of hydrogen.

Acknowledgements

This work was supported by the National Key R&D Program of China (No. 2020YFA0406102), the National Natural Science Foundation of China (grant number 22272078, 91963121), the Natural Science Foundation of Jiangsu Province (Grant No. BK20190056), and the Frontiers Science Center for Critical Earth Material Cycling of Nanjing University. Parts of the calculations were performed using computational resources on an IBM Blade cluster system from the High-Performance Computing Center (HPCC) of Nanjing University.

Conflict of Interest

The authors declare no conflict of interest.

Data Availability Statement

The data that support the findings of this study are available from the corresponding author upon reasonable request.

Keywords: CO_2 reduction · redox stabilization · electrocatalysts · nanostructures · intermediate binding optimization

[1] a) T. T. Zheng, C. X. Liu, C. X. Guo, M. L. Zhang, X. Li, Q. Jiang, W. Q. Xue, H. L. Li, A. W. Li, C. W. Pao, J. P. Xiao, C. A. Xia, J. Zeng, *Nat. Nanotechnol.* **2021**, *16*, 1386–1394; b) P. De Luna, R. Quintero-Bermudez, C. T. Dinh, M. B. Ross, O. S. Bushuyev, P. Todorovic, T. Regier, S. O. Kelley, P. D. Yang, E. H. Sargent, *Nat. Catal.* **2018**, *1*, 103–110; c) M. Zhong, K. Tran, Y. M. Min, C. H. Wang, Z. Y. Wang, C. T. Dinh, P. De Luna, Z. Q. Yu, A. S. Rasouli, P. Brodersen, S. Sun, O. Voznyy, C. S. Tan, M. Askerka, F. Che, M. Liu, A. Seifitokaldani, Y. J. Pang, S. C. Lo, A. Ip, Z. Ulissi, E. H. Sargent, *Nature* **2020**, *581*, 178–183.

[2] a) M. Zhong, T. Hisatomi, Y. B. Kuang, J. Zhao, M. Liu, A. Iwase, Q. X. Jia, H. Nishiyama, T. Minegishi, M. Nakabayashi, N. Shibata, R. Niishiro, C. Katayama, H. Shibano, M. Katayama, A. Kudo, T. Yamada, K. Domen, *J. Am. Chem. Soc.* **2015**, *137*, 5053–5060; b) D. Wakerley, S. Lamaison, J. Wicks, A. n. Clemens, J. Feaster, D. Corral, S. A. Jaffer, A. b. Sarkar, M. Fontecave, E. B. Duoss, S. Baker, E. H. Sargent, T. F. Jaramillo, C. Hahn, *Nat. Energy* **2022**, *7*, 130–143.

[3] a) Y. Cao, B. Wulan, B. H. Zhang, D. X. Tan, J. T. Zhang, *J. Mater. Chem. A* **2021**, *9*, 14741; b) S. Liua, F. J. Pang, Q. W. Zhang, R. J. Guo, Z. F. Wang, Y. C. Wang, W. Q. Zhang, J. Z. Ou, *Appl. Mater. Today* **2018**, *13*, 135–143; c) H. S. Hu, L. Q. Gui, W. Zhou, J. Sun, J. M. Xu, Q. Wang, B. B. He, L. Zhao, *Electrochim. Acta* **2018**, *285*, 70–77; d) P. Zhu, H. T. Wang, *Nat. Catal.* **2021**, *4*, 943–951; e) M. G. Kibria, J. P. Edwards, C. M. Gabardo, C. T. Dinh, A. Seifitokaldani, D. Sinton, E. H. Sargent, *Adv. Mater.* **2019**, *31*, 1807166.

[4] a) L. Li, A. Ozden, S. Y. Guo, A. d. A. F. P. Garci, C. H. Wang, M. Z. Zhang, J. Zhang, H. Y. Jiang, W. Wang, H. Dong, D. Sinton, E. H. Sargent, M. Zhong, *Nat. Commun.* **2021**, *12*, 5223; b) Y. H. Chen, M. W. Kanan, *J. Am. Chem. Soc.* **2012**, *134*, 1986–1989; c) J. T. Feaster, C. Shi, E. R. Cave, T. Hatsukade, D. N. Abram, K. P. Kuhl, C. Hahn, J. K. Norskov, T. F. Jaramillo, *ACS Catal.* **2017**, *7*, 4822–4827.

[5] a) L. Fan, Z. Xia, M. J. Xu, Y. Y. Lu, Z. J. Li, *Adv. Funct. Mater.* **2018**, *28*, 1706289; b) S. Oro, K. Urita, I. Moriguchi, *J. Phys. Chem. C* **2016**, *120*, 25717–25724; c) M. F. Baruch, J. E. Pander, J. L. White, A. B. Bocarsly, *ACS Catal.* **2015**, *5*, 3148–3156; d) F. M. Hassan, Z. W. Chen, A. P. Yu, Z. Chen, X. C. Xiao, *Electrochim. Acta* **2013**, *87*, 844–852.

[6] F. C. Lei, W. Liu, Y. F. Sun, J. Q. Xu, K. T. Liu, L. Liang, T. Yao, B. Pan, S. Q. Wei, Y. Xie, *Nat. Commun.* **2016**, *7*, 12697.

[7] L. Fan, C. Xia, P. Zhu, Y. Y. Lu, H. T. Wang, *Nat. Commun.* **2020**, *11*, 3633.

[8] G. Wen, D. U. Lee, B. Ren, F. M. Hassan, G. Jiang, Z. P. Cano, J. Gostick, E. Croiset, Z. Bai, L. Yang, Z. Chen, *Adv. Energy Mater.* **2018**, *8*, 1802427.

[9] K. Ye, Z. Zhou, J. Shao, L. Lin, D. Gao, N. Ta, R. Si, G. X. Wang, X. H. Bao, *Angew. Chem.* **2020**, *132*, 4844–4851; *Angew. Chem. Int. Ed.* **2020**, *59*, 4814–4821.

[10] L. Wesley, C. Charles, S. Wang, H. Xin, K. He, Y. Kang, F. Jiao, *J. Am. Chem. Soc.* **2017**, *139*, 1885–1893.

[11] R. He, Y. C. Wang, X. Y. Wang, Z. T. Wang, G. Liu, W. Zhou, L. P. Wen, Q. X. Li, X. P. Wang, X. Y. Chen, J. Zeng, J. G. Hou, *Nat. Commun.* **2014**, *5*, 4327.

[12] G. Kresse, J. Hafner, *Phys. Rev. B* **1994**, *49*, 14251–14269.

[13] a) P. E. Blöchl, *Phys. Rev. B* **1994**, *50*, 17953–17979; b) G. Kresse, D. Joubert, *Phys. Rev. B* **1999**, *59*, 1758–1775.

[14] J. P. Perdew, K. Burke, M. Ernzerhof, *Phys. Rev. Lett.* **1996**, *77*, 3865–3868.

[15] V. Wang, N. Xu, J. C. Liu, G. Tang, W. T. Geng, *Comput. Phys. Commun.* **2021**, *267*, 108033.

[16] A. Klinkova, P. De Luna, C.-T. Dinh, O. Voznyy, E. M. Larin, E. Kumacheva, E. H. Sargent, *ACS Catal.* **2016**, *6*, 8115–8120.

[17] a) J. S. Yoo, R. Christensen, T. Vegge, J. K. Nørskov, F. Studt, *ChemSusChem* **2016**, *9*, 358–363; b) R. Christensen, H. A. Hansen, T. Vegge, *Catal. Sci. Technol.* **2015**, *5*, 4946–4949.

[18] G. Kresse, J. Furthmüller, *Phys. Rev. B* **1996**, *54*, 11169–11186.

[19] J. K. Nørskov, J. Rossmeisl, A. Logadottir, L. Lindqvist, J. R. Kitchin, T. Bligaard, H. Jónsson, *J. Phys. Chem. B* **2004**, *108*, 17886–17892.

Manuscript received: January 2, 2023
Revised manuscript received: February 5, 2023
Version of record online: March 2, 2023